ADVANCED OPTICAL MATERIALS
www.advopticalmat.de

Tuning Phase Purity in Chiral 2D Perovskites

Lucas Scalon, Julius Brunner, Maria Gabriella Detone Guaita, Rodrigo Szostak, Miguel Albaladejo-Siguan, Tim Kodalle, L. Andrés Guerrero-León, Carolin M. Sutter-Fella, Caio C. Oliveira, Yana Vaynzof, and Ana Flavia Nogueira**

The introduction of chiral organic spacers in low-dimensional metal-halide perovskites triggers chiroptical activity, which is appealing for spintronic applications. However, a comprehensive understanding of structure formation and the ability to control phase purity in such materials have yet to be developed. Herein, the impact of processing conditions on the phase purity, microstructure, and chiroptical properties of chiral 2D perovskites is explored. The anisotropic emergence of a 1D perovskite inside the 2D matrix and its dependence on the organic cation chirality, solvent, and thermal annealing conditions are shown. By controlling these parameters, the in-plane conductivity of the films is nearly doubled. Furthermore, it is demonstrated, for the first time, that solvent choice and the spatial configuration of the organic cation can have an impact on the residual lattice strain and the energetic disorder of the system. The fundamentals presented here can help to improve the film deposition methods for low-dimensional chiral perovskites, offering strategies to control phase purity.

1. Introduction

Chirality is a fundamental aspect of life and the understanding of its role in chemical and biological systems had a major role in drug discovery, catalysis, and protein-ligand analysis.[1] Recently, chirality has drawn the attention of the material science community due to the possibility of generating chiro-optical,[2–6] and spin-dependent responses,[7–10] which are interesting for quantum computing, spintronics, and imaging.[4,11,12] In the field of chiral materials, enantioenriched molecules have been used to trigger chiroptical and spintronic properties in metal halide perovskites—a low-cost material for photovoltaic, optoelectronic, and photonic applications.

Metal-halide perovskites (MHPs) with a 3D structure are characterized by the general chemical formula ABX_3, with A representing a monovalent cation (e.g., methylammonium, formamidinium, cesium, etc.), B a divalent metal (e.g., Pb^{2+}, Sn^{2+}), and X a halide anion (e.g., Cl^-, Br^-, I^-). Usually, they are organized at room temperature in a cubic structure of corner-sharing $[BX_6]^{4-}$ octahedra, with the A-site cation occupying the cuboctahedral void formed by eight octahedra (**Figure 1**a). By tuning A, B, and X species it is possible to control the optoelectronic properties of the material.[13–15]

An ingenious way to control the properties of MHPs is by changing their dimensionality from 3D- to 2D-, or 1D structures (Figure 1a–c).[16] This can be obtained by replacing the small A-site cation with a bulkier one (A'-cation) and by controlling the stoichiometry between the A-, A'-, and B-site sources. As a result, one can obtain 2D layered (Figure 1b) and 1D polymeric-like (Figure 1c) perovskites structures with the chemical formula $(R'\text{-}NH_3)_2(A)_{n-1}MX_{3n+1}$ and $(R'\text{-}NH_3)BX_3$, respectively, in which n is an integer that defines the number of lead halide octahedra sheets, and R' is an aromatic or aliphatic organic structure.[17-21] Due to this versatility, it is possible to integrate ammonium-based organic molecules with different molecular backbones,[22,23] functional groups,[24,25] and spatial configuration[5,26-29] into 2D and 1D perovskites. In these molecules, the ammonium moiety binds to the A-site of the perovskite via hydrogen- (H-) bonding with the halides, and the aromatic backbones interact with each other through intermolecular π-stacking or van der Waals interaction. Among the plethora of organic molecules available, the introduction of

L. Scalon, M. G. D. Guaita, C. C. Oliveira, A. F. Nogueira
Institute of Chemistry
University of Campinas (UNICAMP)
Campinas, São Paulo 13083-970, Brazil
E-mail: anafla@unicamp.br

L. Scalon, J. Brunner, M. Albaladejo-Siguan, L. A. Guerrero-León, Y. Vaynzof
Chair for Emerging Electronic Technologies
Technische Universität Dresden
Nöthnitzer Straße 61, 01187 Dresden, Germany
E-mail: yana.vaynzof@tu-dresden.de

L. Scalon, J. Brunner, M. Albaladejo-Siguan, L. A. Guerrero-León, Y. Vaynzof
Leibniz-Institute for Solid State and Materials Research Dresden
Helmholtzstraße 20, 01069 Dresden, Germany

R. Szostak
Brazilian Synchrotron Light Laboratory (LNLS)
Brazilian Center for Research in Energy and Materials (CNPEM)
Campinas, SP 13083-970, Brazil

T. Kodalle, C. M. Sutter-Fella
Molecular Foundry
Lawrence Berkeley National Laboratory
1 Cyclotron Road, Berkeley, CA 94720, USA

The ORCID identification number(s) for the author(s) of this article can be found under https://doi.org/10.1002/adom.202300776

© 2023 The Authors. Advanced Optical Materials published by Wiley-VCH GmbH. This is an open access article under the terms of the Creative Commons Attribution License, which permits use, distribution and reproduction in any medium, provided the original work is properly cited.

DOI: 10.1002/adom.202300776

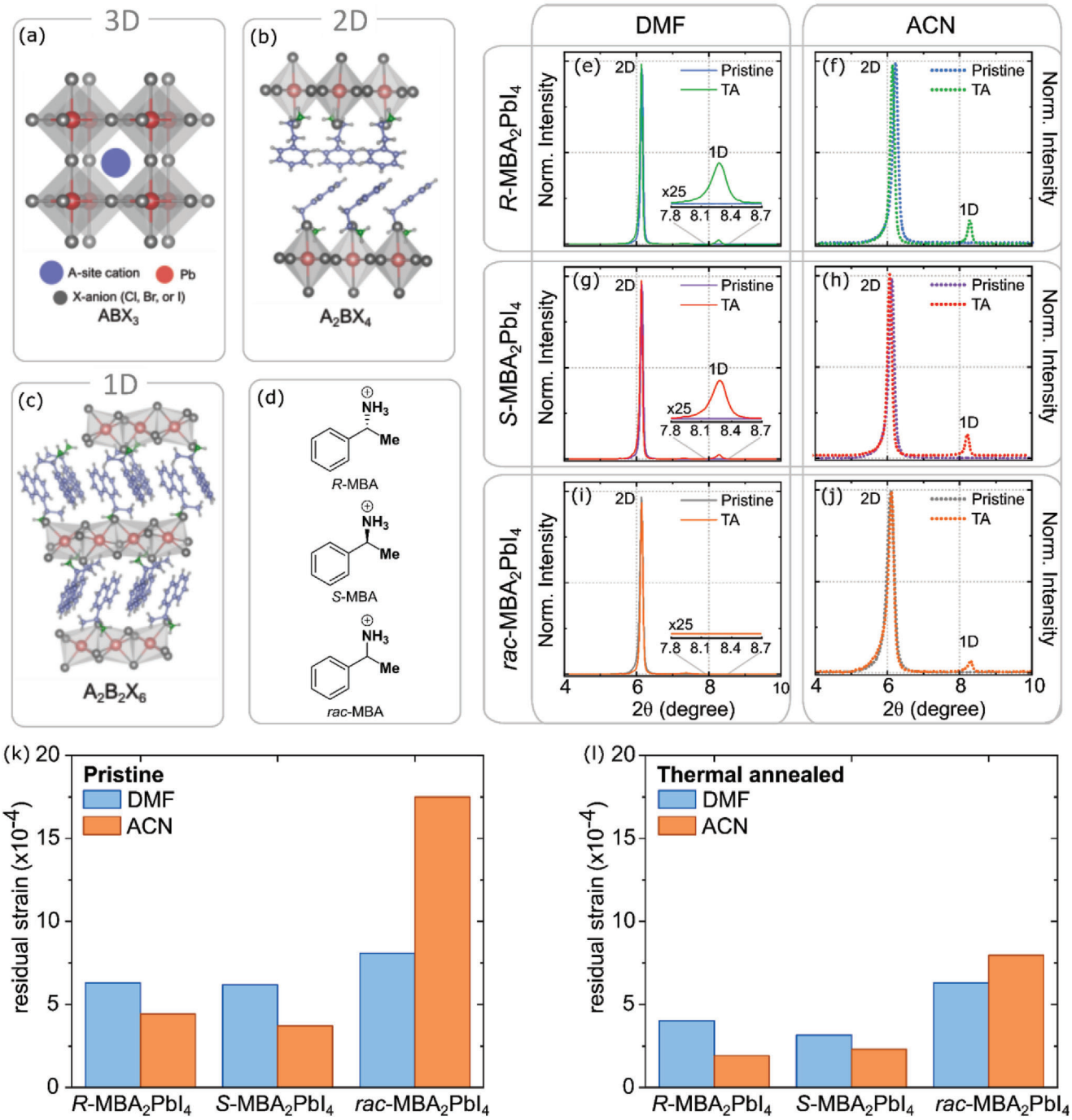

Figure 1. Schematic illustration of a) 3D, b) 2D, and c) 1D perovskites. d) Chemical structure of *R*-, *S*-, and *rac*-methylbenzylammonium (MBA^+) cation. e–j) XRD of *R*-, *S*-, and *rac*-MBA_2PbI_4 thin films prepared from DMF or ACN in the pristine and thermal annealed (TA) conditions. Residual lattice strain for *R*-, *S*-, and *rac*-MBA_2PbI_4 thin films prepared from DMF and ACN in the k) pristine and l) thermal annealed conditions. (b) and (c) were adapted from ref. [31].

chiral organic cations into low-dimensional perovskites is receiving attention since these molecules can break the centrosymmetry operation of the perovskite crystal, and generate chiroptical responses.[30] In these systems, the chirality is transferred from the organic cation to the inorganic $[BX_6]^{4-}$ octahedra layers through asymmetric hydrogen-bonding interaction between the hydrogen of the ammonium group of the chiral molecule and the perovskite's halide.[31] This induces chiroptical responses in these materials,[32] including circular dichroism (CD),[5,26-28] circularly polarized light emission,[10,33-37] and preferential transmission of charge carriers with a specific spin orientation (i.e., chiral-induced spin selectivity effect).[38-40]

© 2023 The Authors. Advanced Optical Materials published by Wiley-VCH GmbH

21951071, 2024, 2, Downloaded from https://onlinelibrary.wiley.com/doi/10.1002/adom.202300776 by Univ of California Lawrence Berkeley National Lab, Wiley Online Library on [24/02/2024]. See the Terms and Conditions (https://onlinelibrary.wiley.com/terms-and-conditions) on Wiley Online Library for rules of use; OA articles are governed by the applicable Creative Commons License

A detailed understanding of film formation processes in such materials is, however, lacking. In general, there are two ways to prepare thin films of low-dimensional perovskites: i) by dissolving the lead source (PbX_2) with the organic ammonium-halide salt in a polar aprotic solvent and ii) by preparing a stoichiometric perovskite powder and solubilizing it in the desired solvent. Strategy (i) is limited by the solubility of the lead source, requiring the use of solvents with a high coordination ability towards Pb^{2+}, e.g., dimethylformamide (DMF). Additionally, it can be difficult to control the stoichiometry of the products in the films, particularly in the preparation of *quasi*-2D ($n \geq 2$) perovskites. Strategy (ii) does not exhibit these issues. Commonly, it is observed that the perovskite powder presents an improved solubility in solvents with less coordination ability with Pb^{2+}, such as acetonitrile (ACN), and the stoichiometry can be better controlled during the synthesis through the addition of stoichiometric amounts of the lead, the A-, and A'-site cations.[41,42] Due to their solubility in a wide variety of organic solvents, the low-dimensional perovskite powders with a controlled stoichiometry can be integrated into layered stacked devices, such as solar cells, to create bulk/low-dimensional perovskite heterojunctions, such as 2D/3D and 1D/3D interfaces, which rely on the sequential deposition of layers of different materials using orthogonal solvents, offering the possibility to obtain a fine control of the phase purity in this type of heterointerface. Such control is difficult to be achieved by the in situ growth of the 2D (or 1D) onto the 3D perovskite using ammonium-based organic cations salts in alcoholic solutions—the most commonly employed method.[43–45]

The interaction between the perovskite precursors (i.e., Pb^{2+}, iodide, and organic cation) and the solvent is crucial to understanding film formation, phase purity, and phase distribution. For instance, when the 2D perovskite powder is dissolved, the solvent molecules coordinate with lead forming complexes of $[PbI_mS_n]^{2-m}$ (where S are the solvent molecules and n and m are integers).[46] The formation and stability of these intermediate complexes depend on the solvent coordination ability, which donates an electron pair to Pb^{2+} ions to form a Lewis adduct.[46-48] During the film formation process, the solvent molecules complexed with lead are replaced by the halide, to form the lead-halide network in which the R'-NH_3^+ species interact with the halide species in the structure through H-bonding interactions. It was demonstrated that these interactions influence the formation rate and the quality of the perovskite film.[49] Therefore, depending on the coordination ability of the solvent with Pb^{2+} and/or the nature of the organic cation, the crystallization pathway can change, potentially resulting in a film comprised of different phases and crystal orientations.

The effects of these interactions are well illustrated when we consider the preparation of 2D perovskite films from powders. Depending on the film preparation conditions and the choice of organic cation, it is possible to observe X-ray diffraction (XRD) features corresponding to 1D polymeric face-sharing lead-halide octahedra chains (Figure 1c) with the chemical formula $A'BX_3$.[26,27,50–53] However, the appearance of this phase is not always discussed. Understanding the phase inhomogeneity is a key point since the 1D phase can impact charge-carrier-dependent properties due to the higher content of insulating organic cations in the 1D phase and the higher lattice separation between the inorganic sheets, which potentially hinders charge transport. Additionally, energy and charge transfer processes from the higher (1D phase) to the lower (2D phase) bandgap material can occur, which can affect the photoluminescence (PL) quantum yield of the system. Furthermore, examining the chiral 2D perovskite literature, one can identify many differences in the XRD features of the racemic mixture compared to the pure enantiomers (*R* and *S*), which includes the appearance of new diffraction peaks, changes in the relative peak intensities, and the values of full width at half maximum (FWHM).[5,26,28,34,50,54] Therefore, it is clear that the spatial orientation of the organic molecule can influence the products obtained and/or the orientation/purity of the phases. However, up to date, and to the best of our knowledge, the influence of the organic cation orientation in the phase purity of low-dimensional perovskite has not been explored.

To explore the film formation processes of chiral 2D perovskites, we investigated the microstructure, morphological and chiroptical properties of *R*-, *S*-, and *rac*-MBA_2PbI_4 (MBA^+: methylbenzylammonium, Figure 1d) 2D perovskites films prepared by mixing the presynthesized perovskite powder in two different solvents: *N*-*N*-dimethylformamide (DMF) and ACN. The choice of those solvents lies in their distinct coordination ability with Pb^{2+}. DMF has a higher coordination ability[55] with Pb^{2+} due to the electron-rich $sp^{[2]}$ oxygen in the amide functional group. In the case of ACN, the nitrogen lone electron pair is localized in the more electronegative sp orbital. For these reasons, the oxygen in DMF is more Lewis basic than the nitrogen in ACN, allowing a stronger interaction with hydrogen bond donors, such as R'-NH_3^+ and the Lewis acidic Pb^{2+}. By preparing chiral 2D perovskite films from these two solvents and analyzing the effect of the thermal annealing condition, we found that the emergence of the 1D perovskite phase, its orientation and distribution over the film are dependent on the solvent, thermal annealing condition, and the spatial configuration of the organic cation. Here, we demonstrate that the control of the 1D phase growth through temperature annealing and solvent can impact the in-plane film conductivity, which may play a role in the future application of these low-dimensional chiral perovskites in transistors, for instance, in which the in-plane charge transport is an important parameter of the device's working mechanism. In addition, we show, for the first time, that the energetic disorder and the residual lattice strain are dependent on the spatial configuration of the organic cation, being higher for the racemic system as compared to the pure enantiomers. Our results point out that the reactivity of the enantiomers is different compared to the racemic mixture, even though these molecules interact with the same achiral substrate, precursors, and solvent molecules.

2. Results and Discussion

2.1. Structural Differences between *R*-, *S*-, and *rac*-MBA_2PbI_4

Crystal powders of *R*-, *S*-, and *rac*-MBA_2PbI_4 were synthesized by adding an appropriate amount of MBA into a solution of PbO in aqueous hydroiodic acid (HI), according to the method described by Moon and co-workers.[26] The detailed procedure is described in the Supporting Information.

As mentioned above, we chose ACN and DMF to examine the formation of the 1D phases as a dependence on the solvent. These two solvents differ significantly in terms of coordination ability

© 2023 The Authors. Advanced Optical Materials published by Wiley-VCH GmbH

21951071, 2024, 2, Downloaded from https://onlinelibrary.wiley.com/doi/10.1002/adom.202300776 by Univ of California Lawrence Berkeley National Lab, Wiley Online Library on [24/02/2024]. See the Terms and Conditions (https://onlinelibrary.wiley.com/terms-and-conditions) on Wiley Online Library for rules of use; OA articles are governed by the applicable Creative Commons License

with Pb^{2+} ions. As shown in Figure S3 in the Supporting Information, ACN forms iodoplumbate species (PbI_n^{2-n}, $n = 2$–6) with a higher iodide content in comparison with DMF, since the latter competes with iodide atoms to vacant Pb^{2+} sites.[46,56,57] As a consequence, the crystallization rate (i.e., film formation) is faster for ACN and suppressed for DMF. Therefore, the choice of solvent is expected to impact the final phase composition and orientation in the film.

Figure 1e–j and Figure S4 in the Supporting Information show the X-ray diffraction pattern of the chiral 2D perovskite films in two regimes of crystallization: the pristine (i.e., the perovskite film was allowed to crystallize spontaneously at room temperature) and thermally annealed (TA, at 100 °C for 10 min) conditions. Independent of the solvent and thermal annealing condition, all the films show a preferential growth in the [*00l*] direction, with peaks at 2θ equal to 6.1°, 12.2°, 18.4°, 24.6°, and ≈31° attributed to the diffraction of (*002*), (*004*), (*006*), (*008*), and (*0010*) planes, respectively. We also observe that, in the TA samples, an additional diffraction peak emerges at $2\theta = 8.3°$ which can be assigned to 1D polymeric face-sharing chains of the *R*-, *S*-, and *rac*-$MBAPbI_3$.[37,58] The presence of the 1D phase can be further confirmed by scanning electron microscopy (SEM) images (Figure S5, Supporting Information) as needle-like crystals appearing in between the 2D grains. In the following sections, we discuss that the distribution and relative orientation of the 1D phase is dependent on the solvent used for film processing, which explains why we observe a decreased amount and less vertically-oriented 1D phase in the case of the DMF-based films. The appearance of the 8.3° peak in the TA ACN-based films may indicate either a temperature-dependent growth or an anisotropic vertical reorientation of the 1D phase.

It is interesting to observe that the relative integrated intensity of the 1D-/2D-related peaks is higher for the ACN-based films compared to those fabricated using DMF. The same tendency is observed for the enantiomeric pure perovskites in comparison to the racemic mixture. For instance, for *R*- and *S*-MBA_2PbI_4 prepared from DMF, the integrated intensity of the 1D phase is ≈2% of the 2D phase, whereas for those films prepared from ACN it is ≈12%. Curiously, for the *rac*-MBA_2PbI_4 prepared from ACN, the 1D peak represents only 5% of the 2D phase intensity, whereas no peak of the 1D phase is observed for the DMF-based samples. These results indicate that the solvent choice, the thermal annealing, and the spatial configuration of the organic cation influence the phase purity of the chiral 2D perovskite films.

In addition to the emergence of the 1D-related peak in the 2D perovskite films, we found that the chirality, solvent, and thermal annealing conditions can also impact the crystallite size (D) and the residual lattice strain (ϵ). Regarding the crystallite size, we observed that DMF-based films always result in larger D-values in comparison to those processed from ACN, which can be attributed to the slow evaporation of the solvent and/or the strong coordination ability of the DMF with the lead complexes, which favors the formation of larger crystalline domains (Table S1, Supporting Information).

Regarding the residual lattice strain, it is known to affect the band structure,[59–61] growth of different materials' structures and phases,[60–62] and the performance and stability of 2D-[63,64] and bulk-based perovskite solar cells.[65,66] Such effects are the result of variations in the Pb-X bonding strength caused by lead octahedra distortions, which influence the electronic properties of the perovskite. The residual strain is commonly related to trigger to the formation of defects in the perovskite layer,[67] besides causing phase instability,[68] inducing ion migration, and accelerating film degradation.[66] Strain can be calculated using the Williamson–Hall equation (Equation (1)),[63,65,69] where β is the FWHM of the XRD peaks, θ is the diffraction angle in rad, $\in$ is the residual strain of the lattice, and K, λ, and D are the Scherrer constant, the X-ray wavelength, and the crystallite size, respectively. Since β and θ can be experimentally obtained, $\in$ can be determined as the angular coefficient of $\beta\cos(\theta)$ versus $[4\sin(\theta)]$ plots; these graphs can be found in Figures S6 and S7 in the Supporting Information, and a summary of the $\in$ values as a dependence of the solvent and TA conditions is shown in Figure 1k,l as well as in Table S1 in the Supporting Information. It is important to mention that the values provided here are relative, and cannot be considered absolute; as such, they can only be compared within the given set of samples. This comparison is assured by the fact that all the X-ray diffractograms were acquired under identical experimental conditions, including the use of the same slit, beam energy, resolution, and other relevant parameters for the XRD measurement. Thus, the experimental contribution to peak broadening can be reasonably assumed to be consistent across all measurements.

$$\beta\cos(\theta) = \in [4\sin\theta] + \frac{K\lambda}{D} \tag{1}$$

We notice that the residual strain decreases for both chiral and racemic mixtures in the TA condition. Curiously, the residual strain of the *rac*-MBA_2PbI_4 is higher compared to the pure enantiomers, regardless of the choice of solvent or crystallization condition. The lattice strain variations may arise from the asymmetric H-bonding interaction that occurs between the ammonium group in the organic cation and the iodide in the lead octahedra, which causes the octahedra to tilt depending on the cation orientation.[31] In the case of the racemic mixture, the fraction of *R*- and *S*- oriented molecules is the same, therefore, part of the lead octahedra will be titled in a given direction and the other part will have a specular tilting, conferring to the racemic perovskite intrinsically higher structural disorder compared to the pure enantiomers. We will demonstrate in the following that this structural disorder of the racemic 2D perovskites also impacts the energetic disorder. We hypothesize that the higher disorder for the racemic 2D perovskite may be the origin of the higher residual strain in those films. In this sense, the use of chiral organic molecules can be an alternative to tune the residual lattice strain in low-dimensional 2D, 1D, and heterointerfaces with bulk perovskites.

2.2. Anisotropic Growth of 1D *R*-, *S*-, and *rac*-$MBAPbI_3$ Perovskite inside 2D Matrix

After establishing the main parameters impacting the formation of the 1D phase in the 2D perovskite we analyzed the distribution and orientation of the 1D phase throughout the film. To access the distribution, XRD at grazing incident angles (Figures S8 and S9, Supporting Information), corresponding to different penetration depths of the X-ray, was recorded, allowing a vertical

© 2023 The Authors. Advanced Optical Materials published by Wiley-VCH GmbH

21951071, 2024, 2, Downloaded from https://onlinelibrary.wiley.com/doi/10.1002/adom.202300776 by Univ of California Lawrence Berkeley National Lab, Wiley Online Library on [24/02/2024]. See the Terms and Conditions (https://onlinelibrary.wiley.com/terms-and-conditions) on Wiley Online Library for rules of use; OA articles are governed by the applicable Creative Commons License

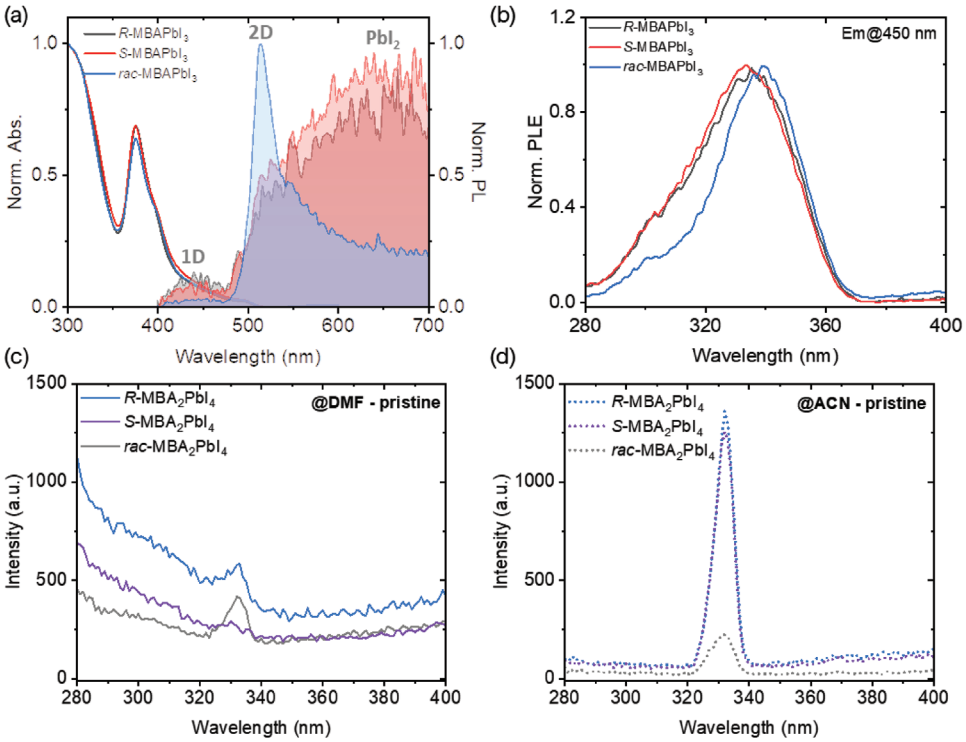

Figure 2. a) UV–vis absorption (empty curve) and PL emission (filled curve) and b) PLE at 450 nm of 1D *R*-, *S*-, and *rac*-MBAPbI$_3$ perovskites. PLE signature of 2D *R*-, *S*-, and *rac*-MBA$_2$PbI$_4$ thin films prepared from c) DMF and d) ACN in the pristine condition.

mapping of the diffraction features in the film. We find that the diffraction corresponding to the 1D perovskite at 8.3° is present even at lower incident angles (0.2°, penetration depth ≈5 nm) in the case of ACN-based films, while for DMF-based films the diffraction obtained at the same incident X-ray angle does not show evidence of the 1D phase. This can indicate either the absence of this phase in the first nanometers of the film—which is consistent with the SEM images of films prepared from DMF, where the 1D phase needle-like structures are less evident (Figure S5, Supporting Information)—or a nonvertical orientation. Such a result suggests that the vertical distribution of the 1D phase is impacted by the choice of solvent. In addition to the previous findings, there is a dependence on the FWHM and the peak position of the 2D-related diffraction peak as the incident angle increases from 0.2° to 1.5°: the former decreases, while the latter shifts to lower 2θ values. These results indicate that the crystal size is increasing deeper in the film and that the interlayer distance between the lead halide octahedra increases, respectively, which may be related to surface effects and/or trapping of residual solvent molecules deep inside the perovskite layer.[70] In summary, these experiments show that the vertical distribution of the 1D phase is impacted by the choice of solvent, but is unaffected by the crystallization condition or cation chirality.

It is important to highlight that the absence of diffraction peaks corresponding to 1D perovskite in the pristine samples does not mean that this phase is not present. This is because conventional XRD is measured along the perpendicular (out-of-plane) direction with respect to the substrate, meaning that domains with different orientations may not be observed. To probe for the presence of the 1D phase in the perovskite films, we measured the photoluminescence excitation (PLE), which is not limited by the orientation of the 1D phase. The PLE can be understood as an absorption spectrum resolved by the emission, i.e., the emission in a specific wavelength is monitored while the excitation energy is varied.[44]

In order to interpret the PLE spectra of the 2D perovskite films we measured the XRD, absorption, emission, and excitation features of the *R*-, *S*-, and *rac*-MBAPbI$_3$ perovskite films (**Figure 2**a,b and Figure S10, Supporting Information). The preparation of these films is described in the Supporting Information. The 1D-perovskite exhibits excitonic absorption at ≈377 nm and emission centered at ≈450 nm (Figure 2a). For the *R*- and *S*- enantiomers, there is also a broad emission band at ≈650 nm, which is attributed to residual PbI$_2$.[71] In the case of the racemic mixture, the 450 nm peak is less evident; however, there are clear signatures of 2D perovskite-related emission at 530 nm. This observation suggests that some 2D phase are formed in the *rac*-1D even though these samples were prepared with a slight excess of PbI$_2$[37] to dislocate the chemical equilibrium towards to formation of the 1D material. The formation of the 2D perovskite is also evidenced in the XRD diffractograms (Figure S10a, Supporting Information). Therefore, the racemic cation tends to trigger the formation of 2D perovskite, whereas the *R*- and *S*-MBA can more easily form the 1D phase. This observation is consistent with our earlier results where a higher amount of 1D phase inside the 2D matrix was observed for the enantiomerically pure chiral perovskites as compared to the racemic mixture (Figure 1e–j). This, once again, illustrates that the spatial orientation of the organic cation can influence the film formation and the products obtained after perovskite crystallization.

© 2023 The Authors. Advanced Optical Materials published by Wiley-VCH GmbH

21951071, 2024, 2, Downloaded from https://onlinelibrary.wiley.com/doi/10.1002/adom.202300776 by Univ of California Lawrence Berkeley National Lab, Wiley Online Library on [24/02/2024]. See the Terms and Conditions (https://onlinelibrary.wiley.com/terms-and-conditions) on Wiley Online Library for rules of use; OA articles are governed by the applicable Creative Commons License

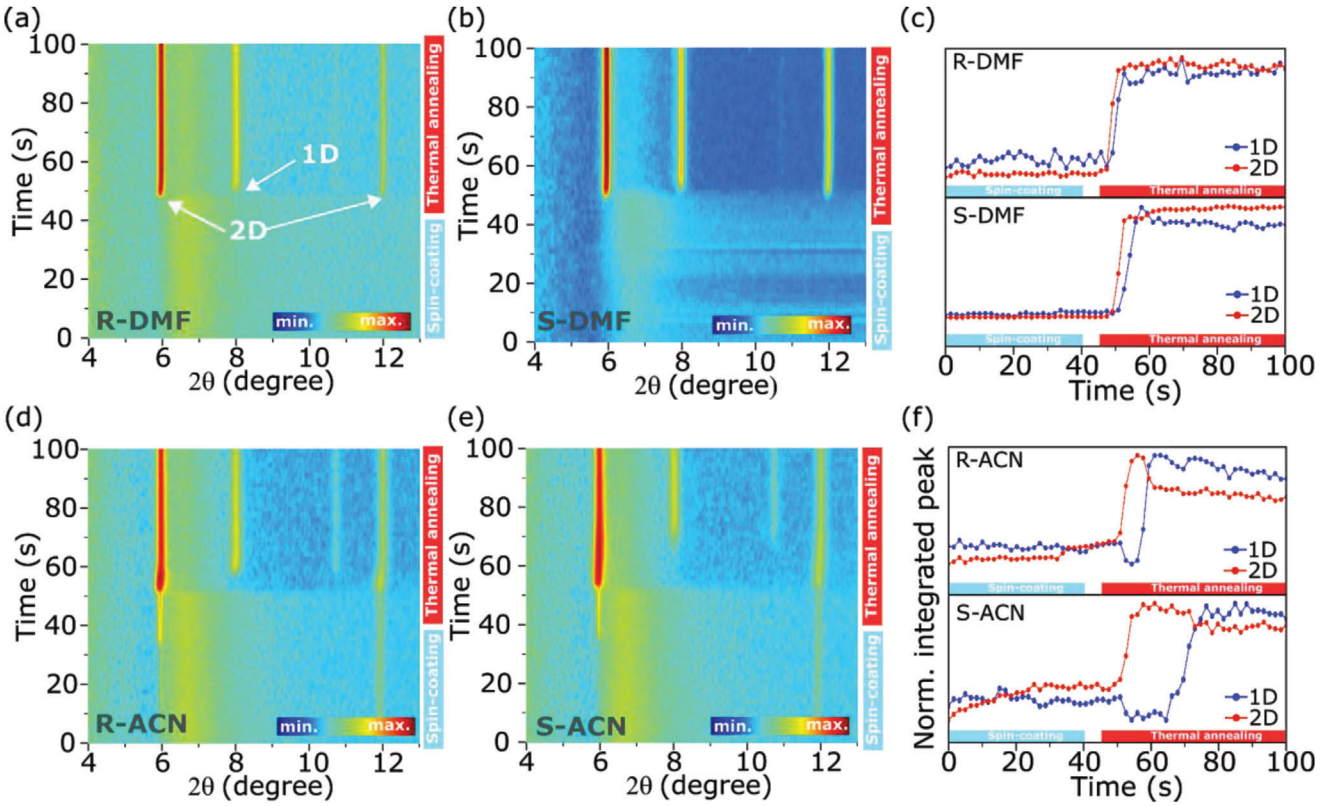

Figure 3. Time-resolved GIWAXS intensity maps (in log scale) of *R*- and *S*-MBA_2PbI_4 thin films prepared from a,b) DMF and d,e) ACN during the spin-coating and thermal annealing steps. Comparison of the normalized integrated peak for the 1D and 2D phases for the *R*- and *S*-MBA_2PbI_4 films prepared from c) DMF and f) ACN.0020.

Since the emission band of the 1D perovskite phase appears at ≈450 nm, we recorded the PLE of the "pure" 1D film following this emission, i.e., the detector was fixed at 450 nm whereas the excitation wavelength was varied from 280–400 nm. The corresponding PLE spectrum reveals one band centered at approximately 330 nm (Figure 2b), which means that the emission at 450 nm originates from species absorbing energy at 330 nm. We also monitored the emission at 500 nm (Figure S10b, Supporting Information)—the emission region of the 2D perovskite—in which it is also possible to identify the presence of the 330 nm band. This indicates that the 1D phase contributes to the emission of the 2D perovskites by energy transfer.[44] In conclusion, the PLE signature at 330 nm can be used to identify the existence of 1D domains in the 2D perovskite films.

PL measurements of the 2D *R*-, *S*-, and *rac*-MBA_2PbI_4 thin films show no direct emission of the 1D phase (Figure S11, Supporting Information), which is consistent with an energy transfer process from the higher bandgap 1D to the lower bandgap 2D phase. By monitoring the PLE in the pristine samples (Figure 2c,d) it was possible to track the signature of the 1D perovskite at about 330 nm. Considering that the photoluminescence quantum yield of the 1D phase is neither affected by the chirality nor by the solvent, it is possible to conclude that the 1D phases are present in the pristine samples. The PLE intensity of the correspondent 1D phase is higher for the ACN compared to the DMF samples, which suggests a higher amount in the film. Since this phase is not detected in the XRD of the samples without thermal annealing for both the solvents tested, we can conclude that TA triggers a reorientation or vertical growth in relation to the substrate of the 1D phase in the system, ultimately resulting in the anisotropic emergence of the 1D perovskite being higher for films prepared from ACN than those prepared from DMF.

Although PLE provided interesting insights into the presence of the 1D phase in the system, it does not offer mechanistic information about the film formation dynamics. To investigate the film formation dynamics and the orientation of the 1D and 2D phases as a dependence of the solvent and chirality of the organic cation, we recorded grazing-incident wide-angle X-ray scattering (GIWAXS) of the *R*- and *S*-MBA_2PbI_4 2D perovskite films prepared from DMF and ACN during spin coating and subsequent thermal annealing (**Figure 3**).

For the samples prepared from DMF, only a broad peak at $2\theta \approx 7\,^{\circ}$ is observed during spin coating, which is attributed to a colloidal sol–gel formed between the solvent and the perovskite precursors (Figure 3a,b). Interestingly, the first crystalline phase to appear is the 2D perovskite just after the onset of thermal annealing. Once the 2D phase starts to form, it reaches the maximum intensity in a short time frame (3–4 s) (Figure 3a,b). It is important to underline that no intermediate species were identified during the formation of the 2D perovskite. This was further confirmed by a similar experiment in which the GIWAXS pattern was recorded without the thermal annealing step and no crystalline phase was observed (Figure S12, Supporting Information).

 © 2023 The Authors. Advanced Optical Materials published by Wiley-VCH GmbH

21951071, 2024, 2, Downloaded from https://onlinelibrary.wiley.com/doi/10.1002/adom.202300776 by Univ of California Lawrence Berkeley National Lab, Wiley Online Library on [24/02/2024]. See the Terms and Conditions (https://onlinelibrary.wiley.com/terms-and-conditions) on Wiley Online Library for rules of use; OA articles are governed by the applicable Creative Commons License

Almost concomitantly with the formation of the 2D phase, with a delay of only 2–3 s, the peak of the 1D phase appears and reaches the maximum intensity very fast (Figure 3c). This behavior is consistent for both *R*- and *S*-MBA_2PbI_4 films prepared from DMF.

For the samples prepared from ACN, just a few seconds after the beginning of the spin-coating a small peak from the 2D phase at $2\theta = 12.0°$ appears (diffraction of the (*004*) plane) (Figure 3d,e). The fastest crystallization of the perovskite is related to the lower boiling point (82 °C for ACN and 153 °C for DMF) and lower coordination ability with Pb^{2+} of ACN compared to DMF evidenced by the presence of iodoplumbate species with lower iodide content for ACN (Figure S3, Supporting Information). During the thermal annealing step, the intensity of the 2D-related peaks, especially for the (*002*) plane, strongly increases. Curiously, the appearance of the 1D phase diffraction emerges after a delay of ≈4–8 s in relation to the 2D—approximately twice as long as in the DMF-based samples.

In summary, the formation of the 2D phase always precedes the 1D, regardless of the choice of solvent or the spatial configuration of the organic cation. Based on that we speculate that the 2D and 1D phases are the kinetic and the thermodynamic products of the film formation reaction, respectively. The hypothesis of the 1D phase being the thermodynamic product is supported by earlier reports regarding the stability of 2D and *quasi*-2D ($n \geq 2$) perovskites.[72,73] It was demonstrated that the formation energy for low *n*-value perovskites is higher compared to high *n*-value 2D phases, which is in agreement with the improved stability for $n = 1$ 2D perovskites when compared to $n \geq 2$.[72,73] This phenomenon is related to the fact that low *n*-value phases have a higher content of bulky organic molecules, which introduces more van der Waals interaction in the system, thereby stabilizing the perovskite.[72,73] Therefore, 1D perovskites are expected to share a similar enhancement in stability. In addition, the linear face-sharing arrangement of the $[BX_6]^{4-}$ octahedra in 1D perovskites improves the strength of the inorganic network in comparison to the 2D, in which the lead-halide octahedra form a corner-connected network.[74,75] Such an arrangement tends to stabilize the Pb^{2+} 6s orbital energy, which typically dominates the valence band of the perovskite.[76,77] conferring thermodynamic stability to the material.[78]

Based on the previous findings, we propose a comprehensive explanation for the formation of both 2D and 1D phases. Our hypothesis is based on two competing processes: PbI_2 and methylbenzylammonium iodide (MBAI) resulting in the 2D phase, and the same reaction leading to the formation of the 1D phase. The former reaction leads to the kinetic product, and, therefore, the associated energetic barrier is smaller compared to the latter. However, we observed that this reaction (i.e., PbI_2 + MBAI ⇌ 2D) seems to be reversible (or *quasi*-reversible), meaning that the 2D phase can be converted into the precursors. Such conversion is mediated by the solvent: as we discussed previously, DMF has a higher coordination ability with lead compared to ACN and, therefore, it can replace iodide atoms in the inorganic 2D network, resulting in the partial dissolution of the structure into the precursor (PbI_2 and MBAI). Thus, the reverse reaction (i.e., 2D to precursors) when DMF is used is facilitated as compared to ACN. This may be the reason why the 1D-related signal in the GIWAXS experiments appears in earlier times for DMF compared to ACN. When the precursors are available, the 1D phase can be formed. Nonetheless, the energetic barrier for its formation is higher compared to the 2D, since this phase only appears after thermal annealing. However, once the 1D phase is formed, it is more stable, meaning that the reverse reaction—from the 1D material to the precursors—is less reversible than in the case of the 2D.

Next, we compare the GIWAXS patterns of the chiral 2D perovskites after the thermal annealing (**Figure 4**a–d). The 2D diffraction images reveal the formation of highly oriented films, with diffraction arcs instead of full rings for DMF and ACN samples. Orientation is however more pronounced for ACN samples, as indicated by analyzing the distribution of intensities along the Debye rings obtained by integrating the GIWAXS data as a function of the polar angle χ (Figure 4e–h). The films prepared from ACN show very narrow peaks for both 1D and 2D phases, whereas, for DMF, the 2D-related diffraction is broader. This suggests that the films prepared from both solvents have the same out-of-plane (q_z) orientation, but such an orientation is improved for the ACN- compared to the DMF-based films. As for the 1D phase, it was found to be less dependent on the solvent, with a similar χ profile for both DMF and ACN. These results highlight the high dependence of the orientation of the 2D phase on the choice of solvent. Therefore, solvent engineering is expected to be a highly important factor for the integration of chiral perovskites into optoelectronic and spintronic devices. In the following, we will demonstrate that the improved out-of-phase orientation obtained by processing from ACN can lead to a significantly higher anisotropic factor in the circular dichroism signal, which is expected to benefit the application of these materials in circular polarized light emission and detection, for example.

To explain the more likely formation of the 2D phase in the case of the racemic mixture when compared to the pure enantiomers (see PLE discussion) one needs to consider the requirements for the formation of the 1D versus 2D and the solubility of the organic cations. If we consider the structures of the 1D and 2D phases, we notice that the former consists of lead iodide octahedra chains bound by the faces and separated by the organic cations (Figure 1c). On the other hand, the latter is formed by lead-halide octahedra sheets connected by the ammonium group of monovalent organic cations, whose tails interact with the adjacent organic cations of another inorganic layer by van der Waals (vdW) interactions (Figure 1b).[79] Hence, vdW interactions between those cations can facilitate (or not) the formation of the 2D over the 1D phase.

The intermolecular interactions between the organic cation can impact the solubility of the 2D perovskite. In the series of organic cations investigated in this study, i.e., *R*-, *S*-, and *rac*-MBA^+, the intermolecular interaction differs between the *R*- (or *S*-) and the racemic mixture due to diastereoselectivity. Previous reports suggest that the introduction of chiral blocks can enhance solubility by reducing efficient packing.[80] As shown in Figure S13 in the Supporting Information, the solubility of the pure enantiomers is indeed higher than that of the racemic mixture. Thus, the nature of the organic cation influences the solubility of the low-dimensional perovskite, which in turn impacts the resulting products after crystallization.

Based on that, we speculate that the lower solubility of the *rac*-MBA_2PbI_4 may facilitate the assembly of 2D perovskite

© 2023 The Authors. Advanced Optical Materials published by Wiley-VCH GmbH

21951071, 2024, 2, Downloaded from https://onlinelibrary.wiley.com/doi/10.1002/adom.202300776 by Univ of California Lawrence Berkeley National Lab, Wiley Online Library on [24/02/2024]. See the Terms and Conditions (https://onlinelibrary.wiley.com/terms-and-conditions) on Wiley Online Library for rules of use; OA articles are governed by the applicable Creative Commons License

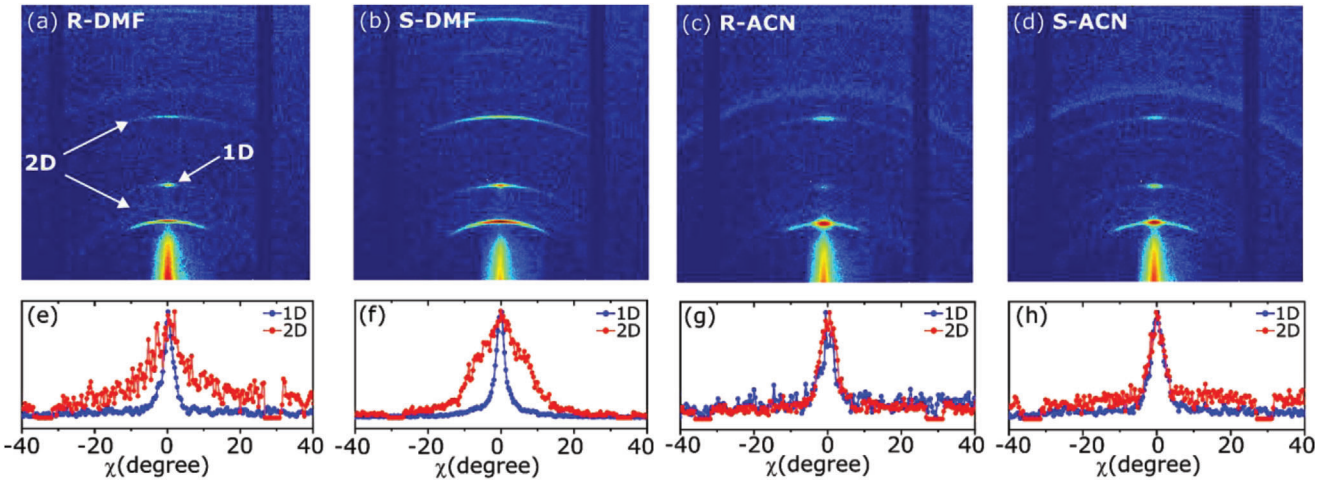

Figure 4. a–d) GIWAXS pattern and e–h) integration over the polar angle χ for of *R*- and *S*-MBA_2PbI_4 perovskite film prepared from DMF and ACN, after the thermal annealing.

structures since the organic molecule may exist as dimers or agglomerates in the precursor solution, favoring the formation of 2D structures. This is because, as explained earlier, the formation of a 2D phase involves an efficient vdW interaction between the organic molecules in the organic cage of the perovskite as well as the interaction between the ammonium group and the lead-octahedra layer, to allow the system assemble in a 2D structure. In contrast, *R*- and *S*-MBA^+ exhibit slightly higher solubility, likely due to their impact on the efficient packing of the crystal. This, in turn, favors the formation of the 1D phase since the vdW interaction between the organic molecules is not as critical for the formation of this phase.

2.3. Impact on Optical Properties, Energetic Disorder, and Conductivity

2.3.1. Photophysical Properties and Energetic Disorder

The absorption and emission features of the *R*-, *S*-, and *rac*-MBA_2PbI_4 prepared from DMF and ACN solutions, in the pristine and TA condition are quite similar (Figure S11 and Tables S2 and S3, Supporting Information), exhibiting excitonic absorption at ≈500 nm and an emission band at ≈530 nm. We notice that the emission band of the MBA-based 2D perovskite is asymmetric, which is in sharp contrast with homologs of low-dimensional perovskites, such as PEA_2PbI_4 (PEA = phenylethylammonium).[81–83] We speculate that this may be related to the formation of additional excited states in the MBA_2PbI_4; however, further investigation is required. The bandgap of the materials, calculated from the onset of the excitonic absorption, shows no dependence on the chirality of the organic molecule or TA condition. Although the spectral shape of the absorption is quite similar, the FWHM of the excitonic peak displays some differences between the pure enantiomers and the racemic mixture (Table S2, Supporting Information). We find that the FWHM of the racemic mixture samples is always slightly higher than the correspondent *R*- and *S*- enantiomers. The FWHM broadening is commonly related to a higher electronic disorder[84] since there are more energetic states available to the excitonic transition.

It is possible to directly evaluate energetic disorder by means of Urbach energy as probed by photothermal deflection spectroscopy (PDS). Such disorder is commonly assigned to either sub-gap states, impurities, or lattice vibrations.[85–87] The Urbach energy (E_U) of the chiral 2D perovskites prepared from ACN and DMF can be calculated using Equation (2), where E is the photon energy and E_g is the optical bandgap. The Urbach energy is related to the exponential increase of the absorption coefficient instead of a sharp transition expected for an "ideal" semiconductor,[88] which occurs because of tail states caused by defects in the crystalline structure and lattice vibrations.[89] Consequently, low values of E_U are related to the high structural quality of the material.[90]

$$\alpha(E) = \alpha_0 \exp\left(\frac{E - E_g}{E_U}\right) \tag{2}$$

Figure 5a,b shows the PDS spectra of *R*-, *S*-, *rac*-MBA_2PbI_4 prepared from DMF and ACN. The values found are similar to previous reports in the literature for PEA_2PbI_4,[91] in which the organic cation is a constitutional isomer of MBA. We find that the E_U for the enantiomeric pure perovskite is lower compared to the racemic analog for both solvents. This trend is similar to what was found for the residual strain, revealing a possible correlation between the higher lattice strain and E_u for the *rac*-MBA_2PbI_4. Also, as expected, the E_U for both *R*- and *S*- enantiomers are the same. Interestingly, the E_U for the 2D films prepared from ACN solvent is more than 3 meV higher compared with the DMF-based films, which may arise due to the presence of a high amount of 1D phase in the ACN-based films. To the best of our knowledge, this is the first time that the Urbach energy of low-dimensional perovskites has been found to depend on the spatial configuration of the organic cation. These results demonstrate that the use of enantiomeric pure organic cations can help to decrease the energetic disorder of 2D perovskite systems. Such a strategy can be applied, for instance, in the fabrication of 2D (1D)/3D perovskite heterointerfaces, in which the lowering of the

© 2023 The Authors. Advanced Optical Materials published by Wiley-VCH GmbH

21951071, 2024, 2, Downloaded from https://onlinelibrary.wiley.com/doi/10.1002/adom.202300776 by Univ of California Lawrence Berkeley National Lab, Wiley Online Library on [24/02/2024]. See the Terms and Conditions (https://onlinelibrary.wiley.com/terms-and-conditions) on Wiley Online Library for rules of use; OA articles are governed by the applicable Creative Commons License

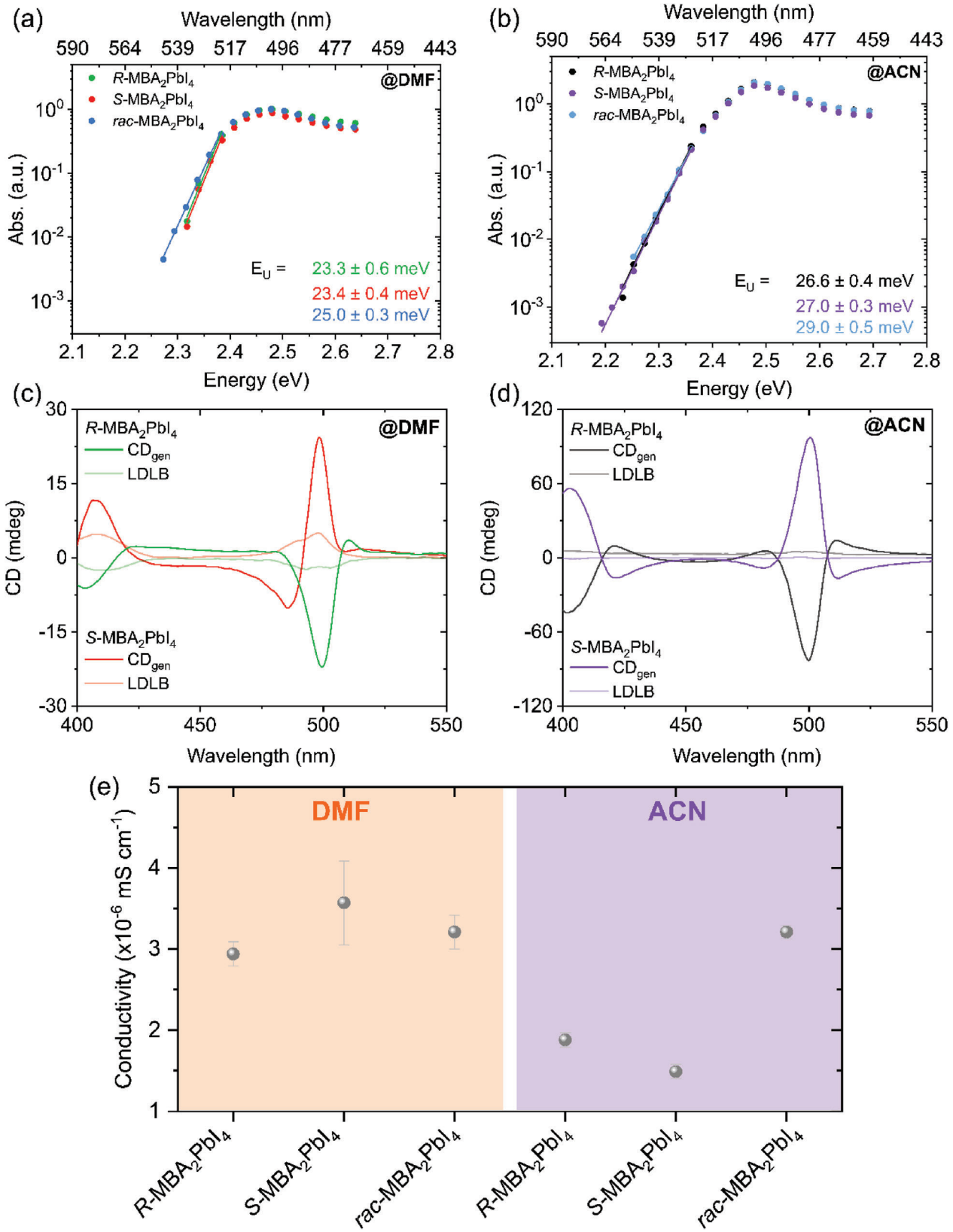

Figure 5. PDS spectra of 2D perovskite films prepared from a) DMF and b) ACN solution. Circular dichroism and anisotropic factor ($g_{factor,CD}$) for *R*- and *S*-MBA_2PbI_4 thin films prepared from c) DMF or d) ACN solution. e) In-plane conductivity measurements of *R*-, *S*-, and *rac*-MBA_2PbI_4 thin films prepared from DMF and ACN.

© 2023 The Authors. Advanced Optical Materials published by Wiley-VCH GmbH

21951071, 2024, 2, Downloaded from https://onlinelibrary.wiley.com/doi/10.1002/adom.202300776 by Univ of California Lawrence Berkeley National Lab, Wiley Online Library on [24/02/2024]. See the Terms and Conditions (https://onlinelibrary.wiley.com/terms-and-conditions) on Wiley Online Library for rules of use; OA articles are governed by the applicable Creative Commons License

energetic disorder has been found to enhance the charge carrier mobility in 2D/3D perovskite heterojunctions.[92]

2.3.2. Circular Dichroism Response

Next, we investigate how the chiroptical response of the system is affected by the solvent. Figure 5c,d and Figures S14 and S15 in the Supporting Information show the CD spectra of the thin films. The anisotropic factor of the CD (g_{factor}) is shown in Figure S16 in the Supporting Information and it was calculated using Equation (3). By using this parameter instead of a direct comparison of CD intensities, we can avoid potential thickness variations from sample to sample which can influence the CD response. In Equation (3), ΔA is the differential absorption obtained from the CD spectra and A is the absorption coefficient obtained from UV–vis measurements. The factor 32 980 is used to make $g_{\text{factor,CD}}$ unitless. The corresponding UV–vis absorption spectra, acquired simultaneously with the CD measurements, are shown in Figures S14 and S15 in the Supporting Information.

$$g_{\text{factor, CD}} = \frac{\Delta A}{A \times 32980} \tag{3}$$

As can be seen from Figure 5c,d, both DMF- and ACN- based films present a derivative line shape changing the sign at the energy corresponding to the excitonic transition of *R*-, *S*-, and *rac*-MBA_2PbI_4 (around 500 nm). This is an observation of the Rashba orbital splitting and occurs because of the splitting of the fundamental electronic transition into two spin-degenerated bands in the *k*-space, each one with a preferential absorption of one given circularly polarized light direction.[31,93-95] The derivative-like line shape for 2D perovskites has also been observed for different perovskite compositions.[96,97] The CD features present slight differences between DMF and ACN, suggesting that solvent choice in the processing of chiral 2D perovskite films impacts the chiroptical response of the system.

It is important to mention that in highly oriented systems, as is the case of the chiral 2D perovskites with a (00*2l*) orientation, the CD signal can be influenced by linear dichroism (LD) and linear birefringence (LB)[96–98] due to interference interaction between the circularly polarized light with macroscopic anisotropies,[99] thereby producing artifactual CD signals. In fact, accounting for the chirality of anisotropic materials is not straightforward, and a simple optical measurement may not be sufficient.[100]

A method for accounting for the presence of LD and LB includes the acquisition of the CD spectra from both the film/air and glass/air interfaces.[97] In the presence of strong LD and LB contributions, the CD signal measured from both sides presents a sign inversion. Such an analysis allows us to determine the linear dichroism plus linear birefringence (LDLB) contribution which can be calculated as $0.5\ x\ (CD_{\text{front}} - CD_{\text{back}})$, and the genuine CD ($CD_{\text{gen}}$), calculated as $0.5\ x\ (CD_{\text{front}} + CD_{\text{back}})$.[96,97,99] As can be seen in Figure 5c,d, the LDLB effect is minimal in our samples. For instance, the ratio between the integrated area of the LDLB and CD_{gen} is < 0.02, for both the ACN- and DMF-based samples, suggesting a low contribution of the macroscopic anisotropies to the CD spectra. We also performed sample rotation measurements from the film/air interface side for the films prepared from DMF and ACN (Figures S14 and S15, Supporting Information). The measurements indicate minimal to no changes in the CD profile, which is in excellent agreement with the LDLB values obtained earlier. In fact, a recent study demonstrated that 2D perovskites are minimally affected by LD and LB since the chirality is mainly due to molecular chirality, and not due to mesoscopic anisotropic domains as observed for 1D materials.[97] Having determined the CD_{gen}, we calculated the genuine anisotropic factor ($g_{\text{factor,genuine}}$) using $\Delta A = CD_{\text{gen}}$ in Equation (3). The results show that films prepared using ACN exhibit a $g_{\text{factor,genuine}}$ in the range of $3 \times 10^{-3} - 5 \times 10^{-3}$, whereas those prepared using DMF show an anisotropy factor lower by approximately one order of magnitude (Figure S16, Supporting Information).

Since the CD signal relies on the magnitude of the lead octahedra distortion caused by the chiral organic cations, different crystal orientations and the presence of different phases (e.g., 1D and 2D) can influence the chiroptical response of the system.[36,97] As shown in the previous sections, ACN triggers the formation of a high amount of 1D phase in the system. An earlier report suggests that the helicity of lead-halide octahedra chains of 1D face-sharing perovskites is more affected by the chiral cations compared to the 2D perovskite.[19] Moreover, the preferred orientation of both the 2D and 1D phases in films prepared from ACN may both contribute to a higher $g_{\text{factor,genuine}}$ observed for the ACN-based films. This is supported by previous reports that demonstrated that CD spectral shape, peak position, and wavelength in which the CD signal crosses zero are all affected by changes in the crystal orientation of the 2D (or 1D) phases.[26,101,102] In light of these results, we demonstrate that the choice of solvent used for the deposition of chiral 2D perovskite thin film impacts the anisotropy factor of CD, which can have implications for the integration of this material in chiroptical devices.

2.3.3. In-Plane Conductivity

In order to demonstrate how the emergence of the 1D phase inside the 2D matrix can influence the properties of the perovskite film, we measured the in-plane (i.e., horizontal) conductivity of the films by fabricating devices with the architecture where Au electrodes are deposited on chiral 2D perovskite on glass. For the pristine condition, the conductivity of the films prepared from DMF and ACN present minimal difference (Figure S17, Supporting Information), even though the crystallite size is slightly different for the two solvents.

For the TA condition (Figure 5e), the DMF-based films present a conductivity almost two times higher when compared to ACN. We note that film thickness does not influence this trend as a similar result is also obtained for DMF and ACN-based films of 350 nm thickness (Figure S18, Supporting Information). As was discussed above, films prepared from DMF have larger crystalline domains as compared to those prepared from ACN, which may explain their higher conductivity. The only exception is the racemic mixture, in which the conductivity is nearly independent of the solvent. This can be due to the similar packing of the *rac*-MBA_2PbI_4 (Figure S5, Supporting Information), even though DMF-based films present a bigger crystallite size, and a lower

© 2023 The Authors. Advanced Optical Materials published by Wiley-VCH GmbH

21951071, 2024, 2, Downloaded from https://onlinelibrary.wiley.com/doi/10.1002/adom.202300776 by Univ of California Lawrence Berkeley National Lab, Wiley Online Library on [24/02/2024]. See the Terms and Conditions (https://onlinelibrary.wiley.com/terms-and-conditions) on Wiley Online Library for rules of use; OA articles are governed by the applicable Creative Commons License

amount (or less oriented) 1D phase, which may benefit the film conductivity. In the case of the enantiomerically pure 2D perovskites, what changes from DMF- to ACN-based films is not just the crystallite size but also the amount and orientation of the 1D perovskite. This phase grows in the *z*-direction, perpendicular to the substrate, in between the grain boundaries of the 2D perovskite (Figure S5, Supporting Information) for the ACN-based samples, thus negatively impacting the in-plane conductivity in the films; this may also be the reason why the conductivity of the pristine films is slightly higher compared to the TA samples.

In general, our results demonstrate that it is possible to control the emergence of the 1D phase in 2D perovskite systems by using a higher lead-coordinating solvent, such as DMF. Moreover, the anisotropic growth of the 1D is highly dependent on the cation chirality and on the crystallization condition (in our case, pristine or TA condition). We anticipate that the control over the formation of the 1D may have important practical application in the future development of chiroptical devices in which in-plane conductivity is an important parameter, such as transistors.

3. Conclusion

We investigated film formation processes in chiral 2D perovskites by utilizing two solvents with different coordination abilities with lead species: DMF and ACN, and the effect of the room temperature- versus temperature-triggered crystallization. Through careful analysis, we have established correlations between solvent, crystallization condition, and spatial configuration of the organic cation with the chiroptical, microstructure, and phase purity of chiral 2D perovskites. We found that a less coordinating solvent, such as acetonitrile, accelerate film formation and triggers the anisotropic orientation of the 1D phase, whereas a highly coordinating solvent, such as dimethylformamide, results in a bigger crystal size with improved control over the phase purity. The formation of the 1D phase was found to impact the in-plane conductivity of the films, which may have important implications in the future development of chiroptic devices. Regarding the effect of the spatial configuration of the organic cation in the *R-, S-*, and *rac*-MBA_2PbI_4, we found that the residual lattice strain and the Urbach energy are higher for the racemic mixture when compared to the enantiomeric pure 2D perovskites. To the best of our knowledge, this is the first time such a correlation is determined. The higher disorder in the *rac*-MBA_2PbI_4 may be related to the lead octahedra tilting induced by the asymmetric H-bonding between the H in the ammonium group of the organic cations with *R* and *S* molecule configuration and the iodide atom in the lead octahedra. Furthermore, we demonstrate the chiroptical response of those perovskites is highly dependent on the solvent choice, with DMF resulting in a lower CD response compared to ACN, which is mainly because the latter triggers an improved out-of-phase orientation of the 2D domains in the film. We expect that these findings enable the development and future integration of chiral perovskites into optoelectronic and spintronic devices.

Supporting Information

Supporting Information is available from the Wiley Online Library or from the author.

Acknowledgements

L.S., M.G.D.G., R.S., and A.F.N. gratefully acknowledge support from FAPESP (São Paulo Research Foundation, Grant Numbers 2017/11986-5 and 2018/21401-7), Shell, and the strategic importance of the support given by ANP (Brazil's National Oil, Natural Gas, and Biofuels Agency) through the R&D levy regulation. L.S. acknowledges FAPESP (grants 2020/04406-5 and 2021/12104-1). R.S. acknowledges FAPESP (grant 2021/01357-6). C.C.O. acknowledges FAPESP (grants 2018/01669-5 and 2014/25770-6). The authors also thank the National Council for Scientific and Technological Development (CNPq) and the Center for Innovation on New Energies (CINE). Y.V. and J.B. thank the Deutsche Forschungsgemeinschaft (DFG) for funding in the framework of the Special Priority Program (SPP 2196) project "PERovskite deFECTs: Physics, eVolution and Stability" (PERFECT PVs) (#424216076). L.A.G.-L. and Y.V. thank the M-ERA.NET project PHANTASTIC (R.8003.22) for funding, supported by the Saxon State Ministry of Science and Art (SMWK). T.K. also thanks the DFG for funding (fellowship number KO6414). This research used resources from the Advanced Light Source, which is a Department of Energy (DOE) Office of Science User Facility under contract no. DE-AC02-05CH11231. This research used facilities of the Brazilian Synchrotron Light Laboratory (LNLS), part of the Brazilian Center for Research in Energy and Materials (CNPEM), a private nonprofit organization under the supervision of the Brazilian Ministry for Science, Technology, and Innovations (MCTI). The Circular Dichroism Beamline (CEDRO) staff is acknowledged for their assistance during the experiments (proposal number 20231710).

Open access funding enabled and organized by Projekt DEAL.

Conflict of Interest

The authors declare no conflict of interest.

Author Contributions

L.S. and Y.V. conceived the idea, designed the experiments, and wrote the original draft. L.S. synthesized the materials, performed characterizations, and analyzed the data. L.S. and L.A.G.-L. performed the in-plane conductivity measurements. J.B. performed the PDS measurements. M.A.S. recorded the SEM images. M.G.D.G., R.S., T.K., and C.M.S-F. performed the GIWAXS experiments. C.C.O., A.F.N., and Y.V. supervised the project. All the authors revised the final version.

Data Availability Statement

The data that support the findings of this study are available from the corresponding author upon reasonable request.

Keywords

chiral organic cations, chiral perovskites, circular dichroism, energetic disorder, film formation, low-dimensional perovskites

Received: March 31, 2023
Revised: July 12, 2023
Published online: July 27, 2023

[1] S. Mason, *Trends Pharmacol. Sci.* **1986**, *7*, 20.
[2] A. Y. Zhu, W. T. Chen, A. Zaidi, Y.-W. Huang, M. Khorasaninejad, V. Sanjeev, C.-W. Qiu, F. Capasso, *Light: Sci. Appl.* **2018**, *7*, 17158.
[3] H. S. Khaliq, I. Kim, A. Zahid, J. Kim, T. Lee, T. Badloe, Y. Kim, M. Zubair, K. Riaz, M. Q. Mehmood, J. Rho, *Photonics Res.* **2021**, *9*, 1667.

© 2023 The Authors. Advanced Optical Materials published by Wiley-VCH GmbH

21951071, 2024, 2, Downloaded from https://onlinelibrary.wiley.com/doi/10.1002/adom.202300776 by Univ of California Lawrence Berkeley National Lab, Wiley Online Library on [24/02/2024]. See the Terms and Conditions (https://onlinelibrary.wiley.com/terms-and-conditions) on Wiley Online Library for rules of use; OA articles are governed by the applicable Creative Commons License

[4] W. Li, Z. J. Coppens, L. V. Besteiro, W. Wang, A. O. Govorov, J. Valentine, *Nat. Commun.* **2015**, *6*, 8379.
[5] G. Long, C. Jiang, R. Sabatini, Z. Yang, M. Wei, L. N. Quan, Q. Liang, A. Rasmita, M. Askerka, G. Walters, X. Gong, J. Xing, X. Wen, R. Quintero-Bermudez, H. Yuan, G. Xing, X. R Wang, D. Song, O. Voznyy, M. Zhang, S. Hoogland, W. Gao, Q. Xiong, E H. Sargent, *Nat. Photonics* **2018**, *12*, 528.
[6] G. Long, G. Adamo, J. Tian, M. Klein, H. N. S. Krishnamoorthy, E. Feltri, H. Wang, C. Soci, *Nat. Commun.* **2022**, *13*, 1551.
[7] R. Gutierrez, E. Díaz, R. Naaman, G. Cuniberti, *Phys. Rev. B* **2012**, *85*, 081404.
[8] Y. Huang, T. Xiao, Z. Xie, J. Zheng, Y. Su, W. Chen, K. Liu, M. Tang, P. Müller-Buschbaum, L. Li, *Adv. Opt. Mater.* **2021**, *9*, 2001663.
[9] A. K. Mondal, M. D. Preuss, M. L. Ślęczkowski, T. K. Das, G. Vantomme, E. W. Meijer, R. Naaman, *J. Am. Chem. Soc.* **2021**, *143*, 7189.
[10] Y.-H. Kim, Y. Zhai, H. Lu, X. Pan, C. Xiao, E. A. Gaulding, S P. Harvey, J. J. Berry, Z. V. Vardeny, J. M. Luther, M. C. Beard, *Science* **2021**, *371*, 1129.
[11] J. Ma, H. Wang, D. Li, *Adv. Mater.* **2021**, *33*, 2008785.
[12] J. A. Gupta, R. Knobel, N. Samarth, D. D. Awschalom, *Science* **2001**, *292*, 2458.
[13] H. Lu, A. Krishna, S. M. Zakeeruddin, M. Grätzel, A. Hagfeldt, *iScience* **2020**, *23*, 101359.
[14] H. Dong, C. Zhang, X. Liu, J. Yao, Y. S. Zhao, *Chem. Soc. Rev.* **2020**, *49*, 951.
[15] M. Li, T. Liu, Y. Wang, W. Yang, X. Lü, *Matter Radiat. Extremes* **2020**, *5*, 018201.
[16] B. P. Carwithen, T. R. Hopper, Z. Ge, N. Mondal, T. Wang, R. Mazlumian, X. Zheng, F. Krieg, F. Montanarella, G. Nedelcu, M. Kroll, M. A. Siguan, J. M. Frost, K. Leo, Y. Vaynzof, M. I. Bodnarchuk, M. V. Kovalenko, A. A. Bakulin, *ACS Nano* **2023**, *17*, 6638.
[17] G. Long, R. Sabatini, M. I. Saidaminov, G. Lakhwani, A. Rasmita, X. Liu, E. H. Sargent, W. Gao, *Nat. Rev. Mater.* **2020**, *5*, 423.
[18] C. Pipitone, S. Boldrini, A. Ferrario, G. Garcìa-Espejo, A. Guagliardi, N. Masciocchi, A. Martorana, F. Giannici, *Appl. Phys. Lett.* **2021**, *119*, 101104.
[19] A. Ishii, T. Miyasaka, *Sci. Adv.* **2020**, *6*, eabd3274.
[20] R. F. Moral, L. G. Bonato, J. C. Germino, C. Oliveira, R. Kamat, W. X. C. Oliveira, R. Kanat, J. Xu, S. C. J. Tassone, S. D. Stranks, M. F. Toney, A. F. Nogueira, *Chem. Mater.* **2019**, *31*, 9472.
[21] M. Rahil, R. M. Ansari, C. Prakash, S. S. Islam, A. Dixit, S. Ahmad, *Sci. Rep.* **2022**, *12*, 2176.
[22] M. C. Gélvez-Rueda, M. B. Fridriksson, R. K. Dubey, W. F. Jager, W. van der Stam, F. C. Grozema, *Nat. Commun.* **2020**, *11*, 1901.
[23] J. V. Passarelli, C. M. Mauck, S. W. Winslow, C. F. Perkinson, J. C. Bard, H. Sai, K. W. Williams, A. Narayanan, D. J. Fairfield, M. P. Hendricks, W. A. Tisdale, S. I. Stupp, *Nat. Chem.* **2020**, *12*, 672.
[24] F. Zhang, D. H. Kim, H. Lu, J.-S. Park, B. W. Larson, J. Hu, L. Gao, C. Xiao, O. G. Reid, X. Chen, Q. Zhao, P. F. Ndione, J. J. Berry, W. You, A. Walsh, M. C. Beard, K. Zhu, *J. Am. Chem. Soc.* **2019**, *141*, 5972.
[25] X. Zhao, M. L. Ball, A. Kakekhani, T. Liu, A. M. Rappe, Y.-L. Loo, *Nat. Commun.* **2022**, *13*, 3970.
[26] J. Ahn, E. Lee, J. Tan, W. Yang, B. Kim, J. Moon, *Mater. Horiz.* **2017**, *4*, 851.
[27] J. Ahn, S. Ma, J.-Y. Kim, J. Kyhm, W. Yang, J. A. Lim, N. A. Kotov, J. Moon, *J. Am. Chem. Soc.* **2020**, *142*, 4206.
[28] B. Sun, X.-F. Liu, X.-Y. Li, Y. Zhang, X. Shao, D. Yang, H.-L. Zhang, **2020**, *Chem. Mater. 32*, 8914.
[29] J.-T. Lin, D.-G. Chen, L.-S. Yang, T.-C. Lin, Y.-H. Liu, Y.-C. Chao, P.-T. Chou, C.-W. Chiu, *Angew. Chem., Int. Ed* **2021**, *60*, 21434.
[30] L. Scalon, Y. Vaynzof, A. F. Nogueira, C. C. Oliveira, *Cell Rep. Phys. Sci.* **2023**, *4*, 101358.
[31] M. K. Jana, R. Song, H. Liu, D. R. Khanal, S. M. Janke, R. Zhao, C. Liu, Z. V. Vardeny, V. Blum, D. B. Mitzi, *Nat. Commun.* **2020**, *11*, 4699.
[32] T. Sheikh, S. Maqbool, P. K. Rajput, P. Mandal, A. Nag, *Chem. Commun.* **2022**, *58*, 7650.
[33] Y. Qin, F.-F. Gao, S. Qian, T.-M. Guo, Y.-J. Gong, Z.-G. Li, G.-D. Su, Y. Gao, W. Li, C. Jiang, P. Lu, X.-H. Bu, *ACS Nano* **2022**, *16*, 3221.
[34] J. Ma, C. Fang, C. Chen, L. Jin, J. Wang, S. Wang, J. Tang, D. Li, *ACS Nano* **2019**, *13*, 3659.
[35] J. Wang, C. Fang, J. Ma, S. Wang, L. Jin, W. Li, D. Li, *ACS Nano* **2019**, *13*, 9473.
[36] L. Wang, Y. Xue, M. Cui, Y. Huang, H. Xu, C. Qin, J. Yang, H. Dai, M. Yuan, *Angew. Chem., Int. Ed* **2020**, *59*, 6442.
[37] C. Chen, L. Gao, W. Gao, C. Ge, X. Du, Z. Li, Y. Yang, G. Niu, J. Tang, *Nat. Commun.* **2019**, *10*, 1927.
[38] R. Naaman, D. H. Waldeck, *J. Phys. Chem. Lett.* **2012**, *3*, 2178.
[39] J. M. Abendroth, D. M. Stemer, B. P. Bloom, P. Roy, R. Naaman, D. H. Waldeck, P. S. Weiss, P. C. Mondal, *ACS Nano* **2019**, *13*, 4928.
[40] H. Lu, J. Wang, C. Xiao, X. Pan, X. Chen, R. Brunecky, J. J. Berry, K. Zhu, M. C. Beard, Z. V. Vardeny, *Sci. Adv.* **2019**, *5*, eaay0571.
[41] S. Ghimire, C. Klinke, *Nanoscale* **2021**, *13*, 12394.
[42] S. Toso, I. Gushchina, A. G. Oliver, L. Manna, M. Kuno, *ACS Energy Lett.* **2022**, *7*, 4242.
[43] A. A. Sutanto, R. Szostak, N. Drigo, V. I. E. Queloz, P. E. Marchezi, J. C. Germino, H. C. N. Tolentino, M. K. Nazeeruddin, A. F. Nogueira, G. Grancini, *Nano Lett.* **2020**, *20*, 3992.
[44] T. Kodalle, R. F. Moral, L. Scalon, R. Szostak, M. Abdelsamie, P. E. Marchezi, A. F. Nogueira, C. M. Sutter-Fella, *Adv. Energy Mater.* **2022**, https://doi.org/10.1002/aenm.202201490.
[45] M. S. de Holanda, R. Szostak, P. E. Marchezi, L. G. T. A. Duarte, J. C. Germino, T. D. Z. Atvars, A. F. Nogueira, *Sol. RRL* **2019**, *3*, 1900199.
[46] E. Radicchi, E. Mosconi, F. Elisei, F. Nunzi, F. De Angelis, *ACS Appl. Energy Mater.* **2019**, *2*, 3400.
[47] A. A. Petrov, I. P. Sokolova, N. A. Belich, G. S. Peters, P. V. Dorovatovskii, Y. V. Zubavichus, V. N. Khrustalev, A. V. Petrov, M. Grätzel, E. A. Goodilin, A. B. Tarasov, *J. Phys. Chem. C* **2017**, *121*, 20739.
[48] J. S. Manser, M. I. Saidaminov, J. A. Christians, O. M. Bakr, P. V. Kamat, *Acc. Chem. Res.* **2016**, *49*, 330.
[49] J.-W. Lee, Z. Dai, C. Lee, H. M. Lee, T.-H. Han, N. De Marco, O. Lin, C. S. Choi, B. Dunn, J. Koh, D. Di Carlo, J. H. Ko, H. D. Maynard, Y. Yang, *J. Am. Chem. Soc.* **2018**, *140*, 6317.
[50] A. Shpatz Dayan, M. Wierzbowska, L. Etgar, *Small Struct.* **2022**, *3*, 2200051.
[51] Y. Lu, Q. Wang, R. Chen, L. Qiao, F. Zhou, X. Yang, D. Wang, H. Cao, W. He, F. Pan, Z. Yang, C. Song, *Adv. Funct. Mater.* **2021**, *31*, 2104605.
[52] Y.-L. Zeng, X.-Q. Huang, C.-R. Huang, H. Zhang, F. Wang, Z.-X. Wang, *Angew. Chem., Int. Ed* **2021**, *60*, 10730.
[53] C. U. Lee, S. Ma, J. Ahn, J. Kyhm, J. Tan, H. Lee, G. Jang, Y. S. Park, J. Yun, J. Lee, J. Son, J.-S. Park, J. Moon, *J. Am. Chem. Soc.* **2022**, *144*, 16020.
[54] Y. Zhao, M. Dong, J. Feng, J. Zhao, Y. Guo, Y. Fu, H. Gao, J. Yang, L. Jiang, Y. Wu, *Adv. Opt. Mater.* **2022**, *10*, 2102227.
[55] Y. Deng, C. H. Van Brackle, X. Dai, J. Zhao, B. Chen, J. Huang, *Sci. Adv.* **2019**, *5*, eaax7537.
[56] L. Liu, J. Lu, H. Wang, Z. Cui, G. Giorgi, Y. Bai, Q. Chen, *Mater. Rep.: Energy* **2021**, *1*, 100064.
[57] S. Rahimnejad, A. Kovalenko, S. M. Forés, C. Aranda, A. Guerrero, *ChemPhysChem* **2016**, *17*, 2795.
[58] D. G. Billing, A. Lemmerer, *CrystEngComm* **2006**, *8*, 686.
[59] L. Zhang, W. Geng, C.-J. Tong, X. Chen, T. Cao, M. Chen, *Sci. Rep.* **2018**, *8*, 7760.
[60] C. Grote, R. F. Berger, *J. Phys. Chem. C* **2015**, *119*, 22832.

© 2023 The Authors. Advanced Optical Materials published by Wiley-VCH GmbH

21951071, 2024, 2, Downloaded from https://onlinelibrary.wiley.com/doi/10.1002/adom.202300776 by Univ of California Lawrence Berkeley National Lab, Wiley Online Library on [24/02/2024]. See the Terms and Conditions (https://onlinelibrary.wiley.com/terms-and-conditions) on Wiley Online Library for rules of use; OA articles are governed by the applicable Creative Commons License

[61] Y. Chen, Y. Lei, Y. Li, Y. Yu, J. Cai, M.-H. Chiu, R. Rao, Y. Gu, C. Wang, W. Choi, H. Hu, C. Wang, Y. Li, J. Song, J. Zhang, B. Qi, M. Lin, Z. Zhang, A. E. Islam, B. Maruyama, S. Dayeh, L.-J. Li, K. Yang, Y.-H. Lo, S. Xu, *Nature* **2020**, *577*, 209.
[62] X. Zheng, C. Wu, S. K. Jha, Z. Li, K. Zhu, S. Priya, *ACS Energy Lett.* **2016**, *1*, 1014.
[63] Q. Cheng, B. Wang, G. Huang, Y. Li, X. Li, J. Chen, S. Yue, K. Li, H. Zhang, Y. Zhang, H. Zhou, *Angew. Chem., Int. Ed* **2022**, *61*, e202208264.
[64] B. Wang, S. Bi, Q. Cheng, G. Huang, W. Zhang, B. Han, Y. Yang, Y. Zhang, H. Zhang, H. Zhou, *Sol. RRL* **2022**, *7*, 2201032.
[65] G. Kim, H. Min, K. S. Lee, D. Y. Lee, S. M. Yoon, S. I. Seok, *Science* **2020**, *370*, 108.
[66] J. Zhao, Y. Deng, H. Wei, X. Zheng, Z. Yu, Y. Shao, J. E. Shield, J. Huang, *Sci. Adv.* **2017**, *3*, eaao5616.
[67] H.-S. Kim, N.-G. Park, *NPG Asia Mater.* **2020**, *12*, 78.
[68] M. I. Saidaminov, J. Kim, A. Jain, R. Quintero-Bermudez, H. Tan, G. Long, F. Tan, A. Johnston, Y. Zhao, O. Voznyy, E. H. Sargent, *Nat. Energy* **2018**, *3*, 648.
[69] G. K. Williamson, W. H. Hall, *Acta Metall.* **1953**, *1*, 22.
[70] B. Yang, D. Bogachuk, J. Suo, L. Wagner, H. Kim, J. Lim, A. Hinsch, G. Boschloo, M. K. Nazeeruddin, A. Hagfeldt, *Chem. Soc. Rev.* **2022**, *51*, 7509.
[71] M. Baibarac, N. Preda, L. Mihut, I. Baltog, S. Lefrant, J. Y. Mevellec, *J. Phys.: Condens. Matter* **2004**, *16*, 2345.
[72] J. Xing, Y. Zhao, M. Askerka, L. N. Quan, X. Gong, W. Zhao, J. Zhao, H. Tan, G. Long, L. Gao, Z. Yang, O. Voznyy, J. Tang, Z.-H. Lu, Q. Xiong, E. H. Sargent, *Nat. Commun.* **2018**, *9*, 3541.
[73] L. N. Quan, M. Yuan, R. Comin, O. Voznyy, E. M. Beauregard, S. Hoogland, A. Buin, A. R. Kirmani, K. Zhao, A. Amassian, D. H. Kim, E. H. Sargent, *J. Am. Chem. Soc.* **2016**, *138*, 2649.
[74] F. Cao, P. Zhang, L. Li, *Fundam. Res.* **2022**, *2*, 237.
[75] P. Liu, Y. Xian, W. Yuan, Y. Long, K. Liu, N. U. Rahman, W. Li, J. Fan, *Adv. Energy Mater.* **2020**, *10*, 1903654.
[76] L. Gao, I. Spanopoulos, W. Ke, S. Huang, I. Hadar, L. Chen, X. Li, G. Yang, M. G. Kanatzidis, *ACS Energy Lett.* **2019**, *4*, 1763.
[77] N. Yang, C. Zhu, Y. Chen, H. Zai, C. Wang, X. Wang, H. Wang, S. Ma, Z. Gao, X. Wang, J. Hong, Y. Bai, H. Zhou, B.-B. Cui, Q. Chen, *Energy Environ. Sci.* **2020**, *13*, 4344.
[78] J. Fan, Y. Ma, C. Zhang, C. Liu, W. Li, R. E. I. Schropp, Y. Mai, *Adv. Energy Mater.* **2018**, *8*, 1703421.
[79] Y. Xu, M. Wang, Y. Lei, Z. Ci, Z. Jin, *Adv. Energy Mater.* **2020**, *10*, 2002558.
[80] O. E. Y. Kilinkissa, K. K. Govender, N. B. Báthori, *CrystEngComm* **2020**, *22*, 2766.
[81] S. Liu, S. Sun, C. K. Gan, A. G. Del Águila, Y. Fang, J. Xing, T. T. H. Do, T. J. White, H. Li, W. Huang, Q. Xiong, *Sci. Adv.* **2019**, *5*, eaav9445.
[82] K.-Z. Du, Q. Tu, X. Zhang, Q. Han, J. Liu, S. Zauscher, D. B. Mitzi, *Inorg. Chem.* **2017**, *56*, 9291.
[83] J. Yin, R. Naphade, L. Gutiérrez Arzaluz, J.-L. Brédas, O. M. Bakr, O. F. Mohammed, *ACS Energy Lett.* **2020**, *5*, 2149.
[84] V. D'Innocenzo, G. Grancini, M. J. P. Alcocer, A. R. S. Kandada, S. D. Stranks, M. M. Lee, G. Lanzani, H. J. Snaith, A. Petrozza, *Nat. Commun.* **2014**, *5*, 3586.
[85] B. Subedi, C. Li, C. Chen, D. Liu, M. M. Junda, Z. Song, Y. Yan, N. J. Podraza, *ACS Appl. Mater. Interfaces* **2022**, *14*, 7796.
[86] S. Zeiske, O. J. Sandberg, N. Zarrabi, C. M. Wolff, M. Raoufi, F. Peña-Camargo, E. Gutierrez-Partida, P. Meredith, M. Stolterfoht, A. Armin, *J. Phys. Chem. Lett.* **2022**, *13*, 7280.
[87] E. Ugur, M. Ledinský, T. G. Allen, J. Holovský, A. Vlk, S. De Wolf, *J. Phys. Chem. Lett.* **2022**, *13*, 7702.
[88] O. V. Rambadey, A. Kumar, A. Sati, P. R. Sagdeo, *ACS Omega* **2021**, *6*, 32231.
[89] V. M. Caselli, Z. Wei, M. M. Ackermans, E. M. Hutter, B. Ehrler, T. J. Savenije, *ACS Energy Lett.* **2020**, *5*, 3821.
[90] M. Stutzmann, *Philos. Mag. B* **1989**, *60*, 531.
[91] Y. Zhang, R. Wang, Y. Li, Z. Wang, S. Hu, X. Yan, Y. Zhai, C. Zhang, C. Sheng, *J. Phys. Chem. Lett.* **2019**, *10*, 13.
[92] Z. Yang, J. Lai, R. Zhu, J. Tan, Y. Luo, S. Ye, *J. Phys. Chem. C* **2022**, *126*, 12689.
[93] M. K. Jana, R. Song, Y. Xie, R. Zhao, P. C. Sercel, V. Blum, D. B. Mitzi, *Nat. Commun.* **2021**, *12*, 4982.
[94] A. Ben-Moshe, A. Teitelboim, D. Oron, G. Markovich, *Nano Lett.* **2016**, *16*, 7467.
[95] D. Niesner, M. Wilhelm, I. Levchuk, A. Osvet, S. Shrestha, M. Batentschuk, C. Brabec, T. Fauster, *Phys. Rev. Lett.* **2016**, *117*, 126401.
[96] S. Ma, Y.-K. Jung, J. Ahn, J. Kyhm, J. Tan, H. Lee, G. Jang, C. U. Lee, A. Walsh, J. Moon, *Nat. Commun.* **2022**, *13*, 3259.
[97] Z. Zhang, Z. Wang, H. H.-Y. Sung, I. D. Williams, Z.-G. Yu, H. Lu, *J. Am. Chem. Soc.* **2022**, *114*, 22242.
[98] Y. Yao, T. J. Ugras, T. Meyer, M. Dykes, D. Wang, A. Arbe, S. Bals, B. Kahr, R. D. Robinson, *ACS Nano* **2022**, *16*, 20457.
[99] G. Albano, G. Pescitelli, L. Di Bari, *ChemNanoMat* **2022**, *8*, 202200219.
[100] H.-G. Kuball, T. Höfer, *Chirality* **2000**, *12*, 278.
[101] R. Rong, Y. Liu, X. Nie, W. Zhang, Z. Zhang, Y. Liu, W. Guo, *Adv. Sci. (Weinheim, Ger.)* **2023**, *10*, e2206191.
[102] R. Pan, J. Hu, S. Tao, L. Kan, H. Yu, K. Wang, *J. Mater. Chem. C* **2022**, *10*, 16706.

© 2023 The Authors. Advanced Optical Materials published by Wiley-VCH GmbH

21951071, 2024, 2, Downloaded from https://onlinelibrary.wiley.com/doi/10.1002/adom.202300776 by Univ of California Lawrence Berkeley National Lab, Wiley Online Library on [24/02/2024]. See the Terms and Conditions (https://onlinelibrary.wiley.com/terms-and-conditions) on Wiley Online Library for rules of use; OA articles are governed by the applicable Creative Commons License